

1 This is a non-peer-reviewed EarthArXiv preprint

2
3 **Oblique slip on long faults enables a continuum of**
4 **earthquake rupture speeds**

5 Huihui Weng¹ and Jean-Paul Ampuero¹

6 ¹*Université Côte d'Azur, IRD, CNRS, Observatoire de la Côte d'Azur, Géoazur, 250 rue Albert*
7 *Einstein, Sophia Antipolis, 06560 Valbonne, France*

8 **Seismological observations show that large earthquakes span a continuum of rupture speeds,**
9 **ranging from slower than Rayleigh wave speeds to P wave speed, and including speeds that**
10 **are predicted to be unstable by 2D theory. Earthquake rupture speed controls ground shak-**
11 **ing and thus seismic hazard, yet a quantitative model reconciling the observations and basic**
12 **theory is still missing. Here we show that long ruptures with oblique slip can propagate**
13 **steadily at a variety of speeds, even in the range of previously-suggested unstable speeds.**
14 **The obliqueness of slip and the ratio of fracture energy to static energy release rate primar-**
15 **ily control the propagation speed of long ruptures. We find that their effects on rupture speed**
16 **can be well predicted by extending the 3D theory of fracture mechanics to long, mixed-mode**
17 **shear ruptures. The basic model developed here provides a new quantitative framework to**
18 **interpret supershear earthquakes, to constrain the energy ratio of faults based on observed**
19 **earthquake rupture speed and rake angle, and to forecast future rupture speeds and sizes**
20 **based on the observed slip deficit along faults.**

21 Introduction

22 Earthquake rupture speed affects ground shaking and thus seismic hazard, yet the quantitative
23 factors controlling the rupture speed of large earthquakes are still not completely understood and
24 the speeds of some earthquakes remain to be reconciled with basic models. In general, faster
25 ruptures generate stronger ground shaking, near to and far from the fault¹⁻³. A compilation of
26 earthquake rupture speeds estimated from seismological observations⁴⁻¹¹ (Fig 3a) illustrates that
27 most earthquakes propagate at speeds slower than the shear wave speed, v_S , and some^{8,9} at speeds
28 faster than the Eshelby speed, $v_E = \sqrt{2}v_S$ (hereafter called “fast supershear” earthquakes). Re-
29 cent evidence^{4,5} shows that supershear earthquakes can also propagate steadily at sub-Eshelby
30 speed (hereafter called “slow supershear”), which is unexpected from the 2D theory of fracture
31 mechanics¹². Such unexpected speeds have been reported in large earthquakes, whose ruptures are
32 much longer than wide^{13,14}. The propagation of ruptures with large aspect ratio has been stud-
33 ied theoretically in 3D in mode III, corresponding to pure-dip-slip faulting¹⁵. By extending that
34 theory to 3D mode II ruptures, we found that slow supershear speeds are also inadmissible for
35 long, steady, pure-strike-slip earthquakes (Methods A3), as in the 2D theory. However, natural
36 earthquakes generally have oblique slip, with both strike-slip and dip-slip components¹³. A 2D
37 theoretical study¹⁶ suggested that such mixed-mode ruptures can propagate at speeds between the
38 Rayleigh wave speed v_R and v_S , which is a “forbidden zone” for pure mode II rupture. Such speeds
39 have been observed in 3D numerical simulations only during very short transients that would be
40 difficult to observe in nature¹⁷. Here, we show that large mixed-mode earthquakes can propagate
41 steadily at speeds spanning the continuum of speeds observed in nature, including “forbidden” and

42 slow supershear speeds.

43 **Rake angle and energy ratio control rupture speed**

44 The propagation of long mixed-mode ruptures (Fig 1) is controlled primarily by two dimensionless
45 quantities, as deduced by dimensional analysis and confirmed by numerical simulations (Methods
46 A1): the rake angle θ between the initial fault traction and the horizontal direction, and the energy
47 ratio G_c/G_0 between dissipated and potential energies. Here, G_c is the fracture energy dissipated
48 near the rupture front and G_0 is the static energy release rate of mode III subshear ruptures. The
49 latter depends on stress drop and rupture width W , but not on rupture length¹⁵. A third non-
50 dimensional parameter, the ratio L_c/W between the size of the weakening process zone at the
51 rupture tip and the rupture width, has a secondary effect on the asymptotic rupture behavior¹⁸.
52 Five different rupture behaviors emerge in 3D numerical simulations as the two primary control
53 parameters are systematically varied (Fig 2a). We first identify two large classes: self-arresting
54 ruptures decelerate and eventually stop spontaneously, while runaway ruptures propagate unabated
55 through the entire fault and eventually approach a steady rupture speed (Fig 2b). We further classify
56 runaway ruptures according to their steady speed: subshear, “forbidden”, slow-supershear and fast-
57 supershear ruptures.

58 Remarkably, long ruptures can propagate steadily at a variety of speeds faster than the
59 Rayleigh wave speed, even at slow supershear speeds and in the “forbidden” zone (Fig 2b). The
60 steady speed of subshear ruptures is v_R for mode II (strike-slip), v_S for mode III (dip-slip), and

61 lies between the two for mixed mode (oblique slip)¹⁶. The steady speeds of supershear ruptures
 62 lie between v_S and v_P and decrease as the rake angle and energy ratio increase (Fig 2c). The
 63 same rupture behaviours are identified on the basis of the apparent horizontal speed (Methods A2),
 64 a quantity more usually constrained by seismological analyses, except that apparent horizontal
 65 speeds in the “forbidden” zone are not found (Fig S2).

66 The conditions separating the different rupture behaviors can be understood and quantita-
 67 tively predicted by extending the theory of fracture mechanics to 3D mixed-mode long ruptures. A
 68 basic element of the theory is that the energy release rate for mixed-mode rupture is the sum of the
 69 mode II and mode III contributions. For steady subshear ruptures, it is of the form $G^{mix} = G_0 f(\theta)$
 70 (Methods A4). Ruptures are runaway if their energy release rate exceeds the fracture energy,
 71 $G^{mix} > G_c$, otherwise they are self-arresting. Thus the boundary between self-arresting and run-
 72 away ruptures satisfies $G_c = G^{mix}$:

$$G_c/G_0 = f(\theta) = (1 - \nu)^{-1} \cos^2 \theta + \sin^2 \theta \quad (1)$$

73 where $\nu = 0.25$ is Poisson’s ratio, which is in good agreement with our 3D dynamic simulations
 74 results (Fig 2a). For steady supershear ruptures, the energy release rate is of the form $G^{mix} =$
 75 $G_0 f(\theta, v_r)$. The values of $f(\theta, v_r)$ at $v_r = v_E$ and $v_r = v_S$ are determined theoretically (Methods
 76 A4) and, in combination with the steady energy balance $G_c = G^{mix}$, the boundaries between
 77 slow and fast supershear ruptures and between slow supershear and “forbidden” ruptures are well
 78 predicted (Fig 2a).

79 Ruptures with oblique slip can propagate steadily at slow supershear and “forbidden” speeds

80 because their rupture fronts are not vertical but tilted (Fig 2d & S1b). A kinematic model that cap-
81 tures purely geometrical effects, considering an expanding elliptical front with obliquely oriented
82 major axis (Fig S4), qualitatively explains the occurrence of unexpected speeds on long faults but
83 also shows substantial discrepancies with the dynamic model (Methods A6). Fracture dynamics
84 theory provides a mechanical explanation for the existence of steady rupture speeds in the “forbid-
85 den” zone. While the mode III contribution to the energy release rate is negative in the “forbidden”
86 zone, in a tilted mixed-mode rupture front it is compensated by the positive mode II contribution
87 (Methods A4), thus enabling a steady energy balance $G^{mix} = G_c$.

88 **Seismological observations of supershear ruptures**

89 The theory developed here provides a new interpretive framework for supershear earthquakes that
90 suggests a method to constrain the energy ratio G_c/G_0 of faults based on observations of earth-
91 quake rupture speed and rake angle. Model and observations can be compared in terms of rupture
92 speed, rake angle and energy ratio (Fig 3a). All the supershear earthquakes observed so far have
93 rake angles lower than 60° and a continuum of rupture speeds up to v_P . The basic model well
94 explains these earthquake observations and constrains the energy ratios of faults to lie between
95 0.5 and 0.89. For energy ratios smaller than 0.5, supershear speeds are, in theory, allowed over a
96 wider range of rake angles (dashed curves in Fig 3a; Methods A1) but have not been observed in
97 nature (Fig 3a). A recent example of slow supershear rupture is the 2018 Mw7.5 Palu earthquake,
98 which was inferred to propagate steadily at a sub-Eshelby speed ~ 4.1 km/s^{5,19}. Considering the
99 rakes constrained by different studies of the Palu earthquake ($\sim 25^\circ$ ¹⁹, ~ 6 - 15° ¹⁴, and ~ 15 - 17° from

100 USGS and gCMT), such slow supershear rupture requires an energy ratio between 0.75 and 0.85.
101 An alternative interpretation of the unusual speed of this earthquake assumes the presence of a
102 low velocity fault zone²⁰, which remains to be confirmed by local fault studies. The 2013 Mw6.7
103 Okhotsk deep earthquake⁶ and the 1999 Mw7.5 Turkey Izmit earthquake⁷ were estimated to prop-
104 agate at Eshelby speed. This requires values of rake angle and energy ratio near the boundary
105 between slow and fast supershear ruptures. The rake angle of these two events are very close to
106 mode II ruptures^{6,13}. Thus, if these ruptures have a steady Eshelby speed, their energy ratio should
107 be around 0.89 (Fig 2a); if their speed is not steady and the rupture comprises both super-Eshelby
108 and subshear segments, this value is an upper bound on the energy ratio for the fault segments
109 with super-Eshelby speed. An example of fast supershear rupture is the 2001 Mw8.1 Kunlun
110 earthquake⁸. An intermediate portion of the rupture had super-Eshelby speed ~ 5 km/s and rake
111 $\sim 10^\circ$ ¹³, which requires $0.7 < G_c/G_0 < 0.8$.

112 The model presented here also explains the continuum of earthquake rupture speeds, ranging
113 from slower than Rayleigh wave speeds to P wave speed (Fig 3b). For subshear runaway rup-
114 tures, steady propagation at speeds arbitrarily lower than the shear wave speed requires the fracture
115 energy to increase with rupture speed, which can result from velocity-dependent friction¹⁵. Oth-
116 erwise, subshear runaway ruptures accelerate to a rake-dependent steady speed between v_R and
117 v_S and, for a given rupture length, their average rupture speed increases from 0 to v_S as the en-
118 ergy ratio decreases. In the “forbidden”, slow-supershear and fast-supershear regimes, ruptures can
119 propagate steadily at speeds between v_R and v_P , even in the absence of velocity-dependent friction:
120 they are stable because the velocity-dependence of energy release rate can stabilize perturbations

121 of rupture speed (Methods A3).

122 **Implications for physics-based seismic hazard assessment**

123 The fracture mechanics theory of long ruptures developed here provides a physics-based frame-
124 work to relate the time-dependent seismic hazard along large faults to quantities that can be ob-
125 served and monitored, such as seismic coupling (Fig 4). A rupture potential Φ was introduced by
126 Weng and Ampuero¹⁵ to infer the arrest distance of long dip-slip (mode III) ruptures with a given
127 spatial distribution of G_c/G_0 along strike. We adapt their definition to mixed-mode long faults as:

$$\Phi(L_1, L_2) = \int_{L_1}^{L_2} (1 - G_c/G^{mix}) dL/W \quad (2)$$

128 where $G^{mix} = G_0 f(\theta)$ is the energy release rate for mixed-mode steady subshear ruptures and W
129 is the rupture width. The rupture potential serves to anticipate the final size of a rupture: a rupture
130 can propagate over the entire fault segment $[L_1, L_2]$ only if $\Phi(L_1, L_2) > 0$, i.e., if the average of
131 the mixed-mode energy ratio G_c/G^{mix} along the segment is < 1 . In addition, if G_c/G^{mix} is much
132 smaller than 1, such as in the slow-supershear and fast-supershear regimes in Fig. 3b, the rupture
133 of the entire fault segment can be supershear. Therefore, two properties that strongly affect the
134 seismic hazard of a given fault, namely rupture length and speed, can be assessed from estimates
135 of the rake angle θ and the energy ratio G_c/G_0 along the fault. The rake angle can be estimated
136 from geodetic data. We propose below an approach to estimate the energy ratio at each along-strike
137 location on long faults.

138 On the one hand, G_0 on long faults is approximately related to final slip D by $G_0 =$

139 $C\mu D^2/W$, where C is a geometrical factor of order 1 (Methods A5). On the other hand, frac-
 140 ture energy G_c can be estimated from scaling relations as a function of final slip D . Such rela-
 141 tions have been derived over a wide range of earthquake sizes by different approaches: dynamic
 142 earthquake modeling²¹⁻²³, laboratory experiments²⁴, and seismological methods such as kinematic
 143 source inversion^{25,26} (Fig 4a). As a crude first-order approximation, we seek a scaling relation of
 144 the form $G_c \approx BD^n$. Theoretical models with off-fault inelastic dissipation^{1,27} lead to $n = 1$ and
 145 for thermal pressurization²⁵ $n = 2/3$. As we focus here on large earthquakes, we only consider the
 146 data with $D > 0.1$ m. We ignore the data of kinematic source inversions which are likely to over-
 147 estimate the fracture energy due to their over-smoothing of the slip rate function²². Least squares
 148 regression gives $n = 0.7$ and $B = 3$ (the units of G_c and D are MJm^{-2} and m , respectively).

149 The resulting relation between energy ratio and slip is: $G_c/G_0 = BW D^{n-2}/C\mu$. The spatial
 150 distribution of slip deficit rate along a fault can be inferred from geodetic observations²⁸⁻³⁰. Given
 151 an estimate of slip deficit at a future time, a worst-case scenario (largest possible magnitude) is
 152 obtained by assuming all the slip deficit is released by a single large earthquake, i.e., D is set
 153 equal to the slip deficit. Because G_0 depends more strongly than G_c on D ($n < 2$), the energy
 154 ratio G_c/G_0 decreases with increasing slip deficit D . Thus the condition for runaway ruptures
 155 (equation (1)) predicts that fault segments need to accumulate a certain critical slip deficit $D^{run}(\theta)$
 156 to become capable of hosting long runaway ruptures, otherwise they can only host self-arresting
 157 ruptures. Combining the scaling relation of energy ratio versus slip with equation (2) allows to
 158 infer the largest possible rupture size from a slip deficit distribution. As an illustration, the time-
 159 dependent evolution of the segmentation of the central Andes subduction zone in Chile predicted

160 by the model is shown in Fig 4c, and yields a reasonable estimate of return time of a 1960-like
161 mega-earthquake of ~ 360 yrs (250 – 500 yrs, accounting for model uncertainties). Similarly,
162 a minimum slip deficit value $D^{sup}(\theta)$ is required for steady supershear ruptures (Methods A4).
163 The model also implies that, on a given fault, supershear earthquakes should have larger slip than
164 subshear ones.

165 Future efforts to establish robust scaling relations between fracture energy and slip, from
166 synergistic developments of frictional theories, laboratory experiments and seismological obser-
167 vations, should allow to integrate the concepts presented here into earthquake hazard assessment.
168 Concretely, based on the spatial distribution of slip deficit rate inferred from geodetic data, the
169 proposed analysis would allow to partition a fault into segments with different potential behaviors
170 in future earthquakes: self-arresting or runaway, subshear or supershear. By accounting for the fi-
171 nite width of seismogenic zones and the obliqueness of earthquake slip, our findings quantitatively
172 reconcile the observations of earthquake rupture speeds with the basic theory of rupture dynamics
173 while opening new avenues for physics-based seismic hazard assessment.

174 **Methods**

175 **A1. Dynamic rupture simulations.** We set 3D dynamic rupture simulations with oblique slip on
 176 a long fault with finite seismogenic width W embedded in an unbounded, linear elastic, homoge-
 177 neous medium. We use a computational domain large enough to avoid the effects of the reflected
 178 waves from the domain boundaries within the simulation time. We assume a Poisson's ratio ν of
 179 0.25. The shear modulus and S wave speed of the medium are denoted μ and v_S , respectively. The
 180 P wave speed, the Eshelby speed, and the Rayleigh wave speed are $v_P = \sqrt{3}v_S$, $v_E = \sqrt{2}v_S$, and
 181 $v_R = 0.92v_S$, respectively.

182 We use the linear slip-weakening friction law with slip-weakening distance d_c , static strength
 183 τ_s , and dynamic strength τ_d . This is the most simple friction law adopted in computational earth-
 184 quake dynamics, and allows to prescribe a constant fracture energy $G_c = 0.5d_c(\tau_s - \tau_d)$. The
 185 strength values are also fixed because the fault normal stress is constant due to the symmetries of
 186 the problem. For a pure-dip-slip fault (rake angle of 90°), Weng and Ampuero¹⁵ demonstrated that
 187 the key parameter that controls the evolution of rupture speed is the energy ratio G_c/G_0^{III} , where
 188 the energy release rate is $G_0^{III} = \lambda_{III}\Delta\tau^2W/\mu$ and $\Delta\tau = \tau_0 - \tau_d$ is the nominal stress drop and
 189 λ_{III} a geometric factor of order 1. The definition of the mode II energy ratio G_c/G_0^{II} is the same³¹
 190 except for the value of the geometric factor λ_{II} . The energy ratio for purely mode II or purely
 191 mode III (assuming the same stress drop $\Delta\tau$) can be written as:

$$\frac{G_c}{G_0^*} = \frac{1}{2\lambda^*} \frac{L_c}{W} \left[\frac{\Delta\tau}{\tau_s - \tau_d} \right]^{-2}, \quad (3)$$

192 where

$$L_c = \frac{\mu d_c}{\tau_s - \tau_d} \quad (4)$$

193 is a characteristic frictional length proportional to the static cohesive zone size³², $\lambda^* = \lambda_{II}$ for
194 mode II and $\lambda^* = \lambda_{III}$ for mode III. The value of λ_{III} was determined analytically and validated
195 numerically¹⁵: $0.96/\pi$ for a deep buried fault (infinite space, like considered here), $1.92/\pi$ for
196 a surface-breaking fault in a half-space, and between $0.96/\pi$ and $1.92/\pi$ for a buried fault in a
197 half-space. Here, we found numerically for mode II ruptures on a deep buried fault that $\lambda_{II} \approx$
198 $0.96/\pi/(1 - \nu)$, which is similar to the value 0.43 obtained by Weng and Yang³¹. Then we have
199 $\lambda_{II}/\lambda_{III} = (1 - \nu)^{-1}$. In the main text, we denote $G_0 = G_0^{III}$, and thus $G_0^{II} = (1 - \nu)^{-1}G_0$. To
200 prescribe the energy ratio G_c/G_0 , we fix the value of the *cohesive ratio* $L_c/W = 0.25$ and vary
201 the stress ratio $\Delta\tau/(\tau_s - \tau_d)$. Note that here we denote $\Delta\tau$ the absolute amplitude of stress drop.
202 The minimum value of the energy ratio is proportional to the *cohesive ratio*, $G_c/G_0 \propto L_c/W$,
203 and is obtained when the stress drop $\Delta\tau$ equals the strength drop $\tau_s - \tau_d$ (in such extreme case,
204 the P wave from the hypocenter can trigger the rupture of the entire fault, enabling rupture at
205 the P wave speed for all mixed-mode ruptures). Since we consider oblique slip with rake angle
206 θ (the direction between the initial traction vector and the horizontal direction), the initial shear
207 stress, whose amplitude is τ_0 , has an along-strike component $\tau_0 \cos \theta$ and along-dip component
208 $\tau_0 \sin \theta$. Exploiting the symmetries of the problem, we only need to simulate rake angles between
209 0° and 90° . Other values θ' between -180° and 180° can be mapped to the $0-90^\circ$ range as $\theta =$
210 $\min(|\theta'|, 180 - |\theta'|)$. If the absolute initial stress τ_0 is too small compared to the stress drop $\Delta\tau$,
211 the slip direction may be time-dependent inside the cohesive zone¹⁶ and thus the actual fracture

212 energy may be larger than G_c . To have full control on the actual value of the fracture energy, we
213 set up a relatively large initial stress, $\tau_0/\Delta\tau \approx 10$.

214 We prescribe a time-dependent weakening over the nucleation zone of size $L/W = 2$ to
215 nucleate unilateral ruptures at prescribed speeds. Rupture propagation becomes spontaneous out-
216 side the nucleation zone. To study steady supershear ruptures, without focusing on the supershear
217 transition, we set the nucleation speed as $1.1v_S$ or $1.414v_S$. Tests show that the value of the nucle-
218 ation speed does not affect the steady-state supershear speed (Fig S3). To study self-arresting and
219 runaway ruptures, we use a sub-Rayleigh nucleation speed of $0.5v_S$.

220 We use the spectral element software SPECFEM3D^{33–36} for the dynamic simulation. All the
221 simulations are conducted on a medium-scale computing cluster with 64 cores and 384 GB mem-
222 ory. We set the time step based on the Courant-Friedrichs-Lewy stability condition. To guarantee
223 sufficient numerical resolution, we set a grid size much smaller than the characteristic frictional
224 length, i.e., $L_c/\Delta x = 10$. We also test a few models with refined grid, $L_c/\Delta x = 20$, and find their
225 results are the same.

226 **A2. Calculations of rupture speed** We compute two types of rupture speed: depth-averaged real
227 speed v_r and apparent horizontal speed v_r^{hor} (Fig S1a). The real speed is computed at each point
228 on the fault from the gradient of rupture time $t(x_1, x_3)$

$$v_r^{real}(x_1, x_3) = \frac{1}{\sqrt{(\partial t/\partial x_1)^2 + (\partial t/\partial x_3)^2}} \quad (5)$$

229 where x_1 and x_3 are the along-strike and along-dip distances, respectively. The horizontal apparent
 230 speed is based on the horizontal gradient of rupture time:

$$v_r^{hor}(x_1, x_3) = \frac{1}{\partial t / \partial x_1}. \quad (6)$$

231 We averaged the real speed and apparent horizontal speed along depth at each along-strike position.

232 **A3. Energy release rate for in-plane supershear rupture** The 2D theory predicts the energy
 233 release rate of supershear ruptures has the following form³⁷:

$$G = g(v_r) \frac{\Delta\tau^2 L}{\mu} \left(\frac{\Lambda}{L}\right)^{p(v_r)} \quad (7)$$

234 where $g(v_r)$ and $p(v_r)$ are known functions of rupture speed, L is the rupture propagation distance,
 235 and Λ is the size of the dynamic cohesive zone, $\Lambda \propto L_c$. In general, $g(v_r)$ depends on the shape
 236 of the slip-weakening curve³⁷, but in this study the friction law is fixed. In 2D, G increases from 0
 237 at $v_r = v_S$ to its peak value at $v_r = v_E$, and then decreases to 0 at $v_r = v_P$. As $p(v_r) < 1$ for all
 238 speeds between v_S and v_P , $G \propto L^{1-p(v_r)}$ is a monotonously increasing function of L . Hence, for
 239 a constant fracture energy G_c , the rupture speed v_r approaches the P wave speed as L grows. Only
 240 if the fracture energy is scale-dependent in the form $G_c \propto L^{1-p(v_r)}$ can steady supershear ruptures
 241 exist. Otherwise the only admissible steady speed is the P wave speed. For elongated ruptures
 242 in 3D, the theory by Weng and Ampuero¹⁵ predicts that G saturates when the rupture reaches a
 243 finite width W ; it becomes a function of W instead of L . Here, we make heuristic modifications
 244 to equation (7) by replacing L with W :

$$G = g(v_r) \left(\frac{\Lambda}{W}\right)^{p(v_r)} G_0. \quad (8)$$

245 Here $g(v_r)$ differs from the one in the 2D theory by a geometrical factor of order 1. The energy
246 balance $G = G_c$ gives

$$\frac{G_c}{G_0} = g(v_r) \left(\frac{\Lambda}{W} \right)^{p(v_r)} \quad (9)$$

247 We suppose that, like in the 2D case, the right side of the above equation also increases from 0 at
248 $v_r = v_S$ to its peak at $v_r = v_E$, and then decreases to 0 at $v_r = v_P$. This equation of motion of
249 mode II long ruptures predicts that supershear propagation is stable if the energy ratio is below the
250 maximum of the right side of equation 9, which is numerically estimated as $g(v_E) \approx 0.9$ (note that
251 $p(v_E) = 0$). If $G_c/G_0 < 0.9$, there are two mathematical solutions of this equation of motion, one
252 with speed between v_S and v_E and the other between v_E and v_P . Only the latter is stable, because
253 the velocity-decreasing energy release rate provides a negative feedback to any perturbation of
254 rupture speed, which stabilizes steady ruptures. In our 3D purely mode II dynamic simulations,
255 we only observe steady supershear ruptures at speeds between v_E and v_P , which is well explained
256 by the heuristic equation of motion.

257 **A4. Energy release rate for mixed-mode rupture** For mixed-mode ruptures in 3D faults with
258 finite width W , we use a reduced-dimensionality (2.5D) model to derive the energy release rate.
259 The 2.5D model has been proved to be a very good approximation of the 3D elongated rupture
260 model¹⁵. It assumes that the rupture front is nearly vertical. In the 3D dynamic simulations, the
261 angles of mixed-mode rupture front are quite small ($< 10^\circ$) for fast supershear, sub-shear runaway
262 and self-arresting ruptures (Fig 2d). For slow supershear and “forbidden” speeds, the rupture front
263 tilt is substantial and its effects can not be ignored.

264 The energy release rate is the rate of mechanical energy flow into the rupture tip per unit
 265 rupture advance. The stress drop vector (fault-parallel traction change) is approximately parallel
 266 to the slip vector, because we focus on situations with little rake rotation. The total energy release
 267 rate for a mixed-mode is the sum of the mode II and III contributions, which are associated to
 268 the along-strike $\Delta\tau_{str} = \Delta\tau \cos \theta$ and along-dip $\Delta\tau_{dip} = \Delta\tau \sin \theta$ components of stress drop,
 269 respectively:

$$G^{mix} = G^{II} \cos^2 \theta + G^{III} \sin^2 \theta \quad (10)$$

270 where G^{II} and G^{III} denote the energy release rates of purely mode II and III ruptures, respectively,
 271 that would prevail if both modes had the same stress drop $\Delta\tau$.

272 Equation (10) can be understood by a circular shear crack model³⁸. The stress intensity
 273 factors at any point along a static circular rupture front of radius a are

$$K_{II} \propto \Delta\tau \sqrt{a} \cos \omega; \quad K_{III} \propto \Delta\tau \sqrt{a} \sin \omega \quad (11)$$

274 where ω is the angle between the slip direction and the local rupture propagation direction. The
 275 expressions have a similar form at the major axis tip of an elliptical rupture, which can be set
 276 horizontal for analogy to the 2.5D model, provided a is the small axis length. Considering the
 277 energy release rate from each mode is proportional to the square of its stress intensity factor³⁹, the
 278 total energy release rate at the rupture front propagating in the horizontal direction has a similar
 279 form to equation (10).

280

Based on 2.5D models (Methods A1 and A3):

$$G^{II} = \begin{cases} (1 - \nu)^{-1}G_0, & \text{if } v_r < v_R \\ G_{fb}^{II}, & \text{if } v_R < v_r < v_S \\ g(v_r)\left(\frac{\Lambda}{W}\right)^{p(v_r)}G_0, & \text{if } v_S < v_r < v_P \end{cases} \quad (12)$$

281 and

$$G^{III} = \begin{cases} G_0, & \text{if } v_r < v_S \\ G_{Sup}^{III}, & \text{if } v_r > v_S \end{cases} \quad (13)$$

282 where $G_0 = \lambda_{III}\Delta\tau^2W/\mu$ and v_r is the depth-averaged real speed. The 2D analytical solutions of283 G_{fb}^{II} and G_{Sup}^{III} depend on the mathematical assumption^{12,16,40}. One solution suggests that G_{fb}^{II} and284 G_{Sup}^{III} have the same forms as for sub-Rayleigh ruptures but with negative values, which are $G_{fb}^{II} =$ 285 $-(1 - \nu)^{-1}G_0$ and $G_{Sup}^{III} = -G_0$ for 2.5D models. Another solution suggests they equal zero.286 The results of 2D numerical simulations¹⁶ lie between the two theoretical solutions. Therefore,287 we suggest these two theoretical solutions are two end-members and suppose G_{fb}^{II}/G_0 has a value288 between $-(1 - \nu)^{-1}$ and 0 and G_{Sup}^{III}/G_0 has a value between -1 and 0.

289 Self-arresting ruptures occur if the energy release rate of mixed-mode steady ruptures is too

290 small to match the fracture energy, $G_c > G^{mix}$. Runaway ruptures near the boundary with self-291 arresting ruptures have sub-Rayleigh speeds and almost vertical fronts ($< 5^\circ$). Thus the theoretical292 boundary between self-arresting and runaway ruptures corresponds to the condition $G_c = G^{mix}$ 293 evaluated at sub-Rayleigh speeds ($v_r < v_R$):

$$G_c/G_0 = (1 - \nu)^{-1} \cos^2 \theta + \sin^2 \theta. \quad (14)$$

294 The theoretical boundary between fast supershear and slow supershear ruptures is obtained by
 295 evaluating the energy balance $G_c = G^{mix}$ at $v_r = v_E$:

$$G_c = g(v_E)G_0 \cos^2 \theta + G_{Sup}^{III} \sin^2 \theta \quad (15)$$

296 where $(\frac{\Lambda}{W})^{p(v_E)} = 1$ because $p(v_E) = 0$ and we know that $g(v_E) = 0.9$ (Methods A3). We find that
 297 if we set $G_{Sup}^{III}/G_0 = -0.4$ (amid the two end-member analytical solutions) the resulting equation
 298 fits well the Eshelby boundary from our 3D dynamic simulations:

$$G_c/G_0 = 0.9 \cos^2 \theta - 0.4 \sin^2 \theta. \quad (16)$$

299 For the boundary between supershear and subshear regimes, the theoretical relation is

$$G_c = g(v_{S+})\left(\frac{\Lambda}{W}\right)^{p(v_{S+})}G_0 \cos^2 \theta + G_{Sup}^{III} \sin^2 \theta \quad (17)$$

300 where v_{S+} is a rupture speed slightly larger than the S wave speed. Near this boundary, the rupture
 301 front tilts severely, $\sim 30^\circ$ (Fig 2d), thus the effects of tilted rupture front needs to be considered. The
 302 first term on the right side of equation (17) is positive and the second term is non positive. The first
 303 term on the right side of equation (17) need to be sufficient to support the dissipated fracture energy.
 304 As the term $g(v_{S+})$ is quite small according to the theory (Methods A3), we suppose that the
 305 geometrical effect of tilted front enlarges the size of the “apparent cohesive zone” along the strike
 306 direction to make the first term sufficiently large. We find that if we set $g(v_{S+})\left(\frac{\Lambda}{W}\right)^{p(v_{S+})} = 0.9$
 307 (same as equation (16)) and $G_{Sup}^{III}/G_0 = 0.0$ (one end-member analytical solution) the resulting
 308 equation fits well the supershear boundary for small rake angle

$$G_c/G_0 = 0.9 \cos^2 \theta. \quad (18)$$

309 For larger rake angle, equation (18) underestimates the energy release rate due to the even larger
 310 tilt of the rupture front ($>30^\circ$, Fig 2d).

311 **A5. Scaling relation of energy release rate** On long faults, the static energy release rate $G_0(x)$
 312 is related to final slip $D(x)$ by

$$G_0(x) = \frac{1}{2} \int_0^W \Delta\tau(x, z) D(x, z) dz \quad (19)$$

313 where x and z are along-strike and along-dip distances, respectively. To first order, $\Delta\tau(x) =$
 314 $2C\mu D(x)/W$, thus this equation is approximated as

$$G_0(x) = \frac{C\mu D(x)^2}{W} = \frac{1}{4C} \frac{\Delta\tau(x)^2 W}{\mu} \quad (20)$$

315 where C is a geometrical factor of order 1 and $\Delta\tau(x)$ and $D(x)$ are the depth-averaged stress
 316 drop and slip, respectively. For a very long mode III rupture with constant stress drop, the static
 317 factor⁴¹ relating stress drop $\Delta\tau$ and final average slip D on a deep buried fault is $C = \pi/4$.

318 Comparing equation (20) with the definition of mode II energy release rate (Methods A1), we have

319 $C = 1/(\lambda_{III})$, which is consistent with the static factor⁴¹ on a deep buried fault. For mode II

320 rupture, $\lambda_{II}/\lambda_{III} = (1 - \nu)^{-1}$ and thus $C = (1 - \nu)\pi/4$, where ν is the Poisson's ratio. For a

321 mixed-mode rupture,

$$\begin{aligned} \Delta\tau^2 &= \Delta\tau_{str}^2 + \Delta\tau_{dip}^2 \\ \Delta\tau_{str} &= \frac{(1 - \nu)\pi\mu}{4W} D_{str} \\ \Delta\tau_{dip} &= \frac{\pi\mu}{4W} D_{dip}. \end{aligned} \quad (21)$$

322 Since we focus on situations with little rake rotation, we have

$$D_{str} = D \cos \theta \quad (22)$$

$$D_{dip} = D \sin \theta.$$

323 Therefore, the factor relating stress drop $\Delta\tau$ and final average slip D for mixed-mode rupture is

$$C = \frac{\pi}{4} \sqrt{(1 - \nu)^2 \cos^2 \theta + \sin^2 \theta} \quad (23)$$

324 **A6. Kinematic model** To investigate the possible reasons of unexpected steady speeds, we com-
325 pare the dynamic models with a simple kinematic model designed to capture purely-geometric
326 effects (Fig S4a). We assume that a supershear rupture extends as an elliptical front propagating
327 at the P wave speed along its major axis and at the S wave speed along its minor axis, the limiting
328 speeds for mode II and III ruptures, respectively. The elliptical fronts are truncated to lie inside the
329 seismogenic portion of the fault. The rake angle is the angle between the major axis of the ellipse
330 and the strike direction. We vary the rake angle and compute the depth-averaged real speed, the
331 horizontal speed and the depth-averaged rupture propagation angle (angle of the real rupture speed
332 relative to the horizontal direction).

333 We find that the basic geometrical effects of tilted elliptical front represented in the kinematic
334 model only account for part of the dynamic simulation results. The rupture speeds decrease as the
335 rake angle increases (Fig S4b and S4c), as in the dynamic models, but there are also important
336 discrepancies between the two models. Beyond a rake of 20-30°, the speed of the dynamic models
337 decreases faster than that of the kinematic models. An eventual drop to sub-Rayleigh speeds is
338 only found in the dynamic models. Furthermore, the variability of the real speed across the depth

339 profile is larger in the dynamic model than in the kinematic model. The dependency of the rupture
340 propagation angle as a function of rake angle (Fig S4d) is totally different between the two models.
341 Also, the variability across depth of the rupture angle is much larger in the dynamic model than
342 in the kinematic model, which means the curvature of the dynamic front is larger than that of the
343 kinematic elliptical front. The rupture angle drops to less than 10° once the speed drops below the
344 Rayleigh speed, only in the dynamic models.

- 346 1. Gabriel, A., Ampuero, J., Dalguer, L. & Mai, P. M. Source properties of dynamic rupture
347 pulses with off-fault plasticity. *Journal of Geophysical Research* **118**, 4117–4126 (2013).
- 348 2. Dunham, E. M. & Bhat, H. S. Attenuation of radiated ground motion and stresses from three-
349 dimensional supershear ruptures. *Journal of Geophysical Research: Solid Earth* **113** (2008).
- 350 3. Andrews, D. Ground motion hazard from supershear rupture. *Tectonophysics* **493**, 216–221
351 (2010).
- 352 4. Chounet, A., Vallée, M., Causse, M. & Courboux, F. Global catalog of earthquake rupture
353 velocities shows anticorrelation between stress drop and rupture velocity. *Tectonophysics* **733**,
354 148–158 (2018).
- 355 5. Bao, H. *et al.* Early and persistent supershear rupture of the 2018 magnitude 7.5
356 palu earthquake. *Nature Geoscience* (2019). URL [https://doi.org/10.1038/
357 s41561-018-0297-z](https://doi.org/10.1038/s41561-018-0297-z).

- 358 6. Zhan, Z., Helmberger, D. V., Kanamori, H. & Shearer, P. M. Supershear rupture in a mw 6.7
359 aftershock of the 2013 sea of okhotsk earthquake. *Science* **345**, 204–207 (2014).
- 360 7. Bouchon, M. *et al.* How fast is rupture during an earthquake? new insights from the 1999
361 turkey earthquakes. *Geophysical Research Letters* **28**, 2723–2726 (2001).
- 362 8. Bouchon, M. & Vallée, M. Observation of long supershear rupture during the magnitude 8.1
363 kunlunshan earthquake. *Science* **301**, 824–826 (2003).
- 364 9. Yue, H. *et al.* Supershear rupture of the 5 january 2013 craig, alaska (mw 7.5) earthquake.
365 *Journal of Geophysical Research* **118**, 5903–5919 (2013).
- 366 10. Wang, D. & Mori, J. Short-period energy of the 25 april 2015 mw 7.8 nepal earthquake deter-
367 mined from backprojection using four arrays in europe, china, japan, and australia. *Bulletin of*
368 *the Seismological Society of America* **106**, 259–266 (2016).
- 369 11. Hicks, S. *et al.* Back-propagating super-shear rupture in the 2016 m7. 1 romanche transform
370 fault earthquake. *Eartharxiv* (2019).
- 371 12. Burridge, R. Admissible speeds for plane-strain self-similar shear cracks with friction but
372 lacking cohesion. *Geophysical Journal International* **35**, 439–455 (1973).
- 373 13. Mai, P. M. & Thingbaijam, K. Srcmod: An online database of finite-fault rupture models.
374 *Seismological Research Letters* **85**, 1348–1357 (2014).

- 375 14. Song, X. *et al.* Geodetic observations of the 2018 mw 7.5 sulawesi earthquake and its im-
376 plications for the kinematics of the palu fault. *Geophysical Research Letters* **46**, 4212–4220
377 (2019).
- 378 15. Weng, H. & Ampuero, J. The dynamics of elongated earthquake ruptures. *Journal of Geo-*
379 *physical Research: Solid Earth* (2019).
- 380 16. Andrews, D. Dynamic growth of mixed-mode shear cracks. *Bulletin of the Seismological*
381 *Society of America* **84**, 1184–1198 (1994).
- 382 17. Bizzarri, A. & Das, S. Mechanics of 3-d shear cracks between rayleigh and shear wave rupture
383 speeds. *Earth and Planetary Science Letters* **357**, 397–404 (2012).
- 384 18. Ampuero, J. & Mao, X. Upper limit on damage zone thickness controlled by seismogenic
385 depth. *Fault Zone Dynamic Processes: Evolution of Fault Properties During Seismic Rupture*
386 **227**, 243 (2017).
- 387 19. Fang, J. *et al.* The 2018 mw 7.5 palu earthquake: A supershear rupture event constrained by
388 insar and broadband regional seismograms. *Remote Sensing* **11**, 1330 (2019).
- 389 20. Oral, E., Weng, H. & Ampuero, J. P. Does a damaged-fault zone mitigate the near-field im-
390 pact of supershear earthquakes?—application to the 2018 mw 7.5 palu, indonesia earthquake.
391 *Geophysical Research Letters* e2019GL085649 (2020).
- 392 21. Mai, P. *et al.* On scaling of fracture energy and stress drop in dynamic rupture models: Con-
393 sequences for near-source ground-motions. *Earthquakes: Radiated Energy and the Physics of*
394 *Faulting* 283–293 (2006).

- 395 22. Weng, H. & Yang, H. Constraining frictional properties on fault by dynamic rupture simula-
396 tions and near-field observations. *Journal of Geophysical Research* (2018).
- 397 23. Gallovič, F., Valentová, L., Ampuero, J. & Gabriel, A. Bayesian dynamic finite-fault inversion:
398 1. method and synthetic test. *Journal of Geophysical Research: Solid Earth* (2019).
- 399 24. Nielsen, S. *et al.* G: Fracture energy, friction and dissipation in earthquakes. *Journal of*
400 *Seismology* 1–19 (2016).
- 401 25. Viesca, R. C. & Garagash, D. I. Ubiquitous weakening of faults due to thermal pressurization.
402 *Nature Geoscience* **8**, 875–879 (2015).
- 403 26. Tinti, E., Cocco, M., Fukuyama, E. & Piatanesi, A. Dependence of slip weakening distance
404 (dc) on final slip during dynamic rupture of earthquakes. *Geophysical Journal International*
405 **177**, 1205–1220 (2009).
- 406 27. Andrews, D. Rupture dynamics with energy loss outside the slip zone. *Journal of Geophysical*
407 *Research* **110** (2005).
- 408 28. Moreno, M. *et al.* Heterogeneous plate locking in the south–central Chile subduction zone:
409 Building up the next great earthquake. *Earth and Planetary Science Letters* **305**, 413–424
410 (2011).
- 411 29. Jolivet, R., Simons, M., Agram, P., Duputel, Z. & Shen, Z. Aseismic slip and seismogenic cou-
412 pling along the central San Andreas fault. *Geophysical Research Letters* **42**, 297–306 (2015).

- 413 30. Villegas-Lanza, J. C. *et al.* Active tectonics of peru: Heterogeneous interseismic coupling
414 along the nazca megathrust, rigid motion of the peruvian sliver, and subandean shortening
415 accommodation. *Journal of Geophysical Research: Solid Earth* **121**, 7371–7394 (2016).
- 416 31. Weng, H. & Yang, H. Seismogenic width controls aspect ratios of earthquake ruptures. *Geo-*
417 *physical Research Letters* **44**, 2725–2732 (2017).
- 418 32. Day, S., Dalguer, L., Lapusta, N. & Liu, Y. Comparison of finite difference and boundary
419 integral solutions to three-dimensional spontaneous rupture. *Journal of Geophysical Research*
420 **110**, B12307 (2005).
- 421 33. Ampuero, J. Etude physique et numérique de la nucléation des séismes. *PhD Thesis, Univer-*
422 *sity of Paris VII, France* (2002).
- 423 34. Komatitsch, D. & Vilotte, J.-P. The spectral element method: an efficient tool to simulate the
424 seismic response of 2d and 3d geological structures. *Bulletin of the seismological society of*
425 *America* **88**, 368–392 (1998).
- 426 35. Galvez, P., Ampuero, J.-P., Dalguer, L. A., Somala, S. N. & Nissen-Meyer, T. Dynamic
427 earthquake rupture modelled with an unstructured 3-d spectral element method applied to the
428 2011 m 9 tohoku earthquake. *Geophysical Journal International* **198**, 1222–1240 (2014).
- 429 36. Kaneko, Y., Lapusta, N. & Ampuero, J. Spectral element modeling of spontaneous earthquake
430 rupture on rate and state faults: Effect of velocity-strengthening friction at shallow depths.
431 *Journal of Geophysical Research* **113**, B09317 (2008).

- 432 37. Broberg, K. Intersonic bilateral slip. *Geophysical Journal International* **119**, 706–714 (1994).
- 433 38. Tada, H., Paris, P. C., Irwin, G. R. & Tada, H. *The stress analysis of cracks handbook*, vol.
434 130 (ASME press New York, 2000).
- 435 39. Freund, L. *Dynamic fracture mechanics* (Cambridge university press, 1998).
- 436 40. Freund, L. & Clifton, R. On the uniqueness of plane elastodynamic solutions for running
437 cracks. *Journal of elasticity* **4**, 293–299 (1974).
- 438 41. Luo, Y., Ampuero, J.-P., Miyakoshi, K. & Irikura, K. *Surface rupture effects on earthquake*
439 *moment-area scaling relations*, 7–18 (Springer, 2018).

440 **Acknowledgements** The open-source software SPECFEM3D used in our 3-D dynamic rupture simula-
441 tions is available from the Computational Infrastructure for Geodynamics at
442 <https://geodynamics.org/cig/software/specfem3d/>. This work was supported by the French government
443 through the Investments in the Future project UCAJEDI (ANR-15-IDEX-01) managed by the French Na-
444 tional Research Agency (ANR). We thank Diego Molina for providing the central Andes coupling model in
445 digital form.

446 **Correspondence** Correspondence and requests for materials should be addressed to Huihui Weng (email:
447 weng@geoazur.unice.fr).

448 **Figure 1** Long rupture propagating on a fault with finite width W and oblique slip (rake
449 angle defined between slip and strike directions). The inset shows the propagation of a
450 tilted rupture front on a fault, arrows show the local direction of rupture speed.

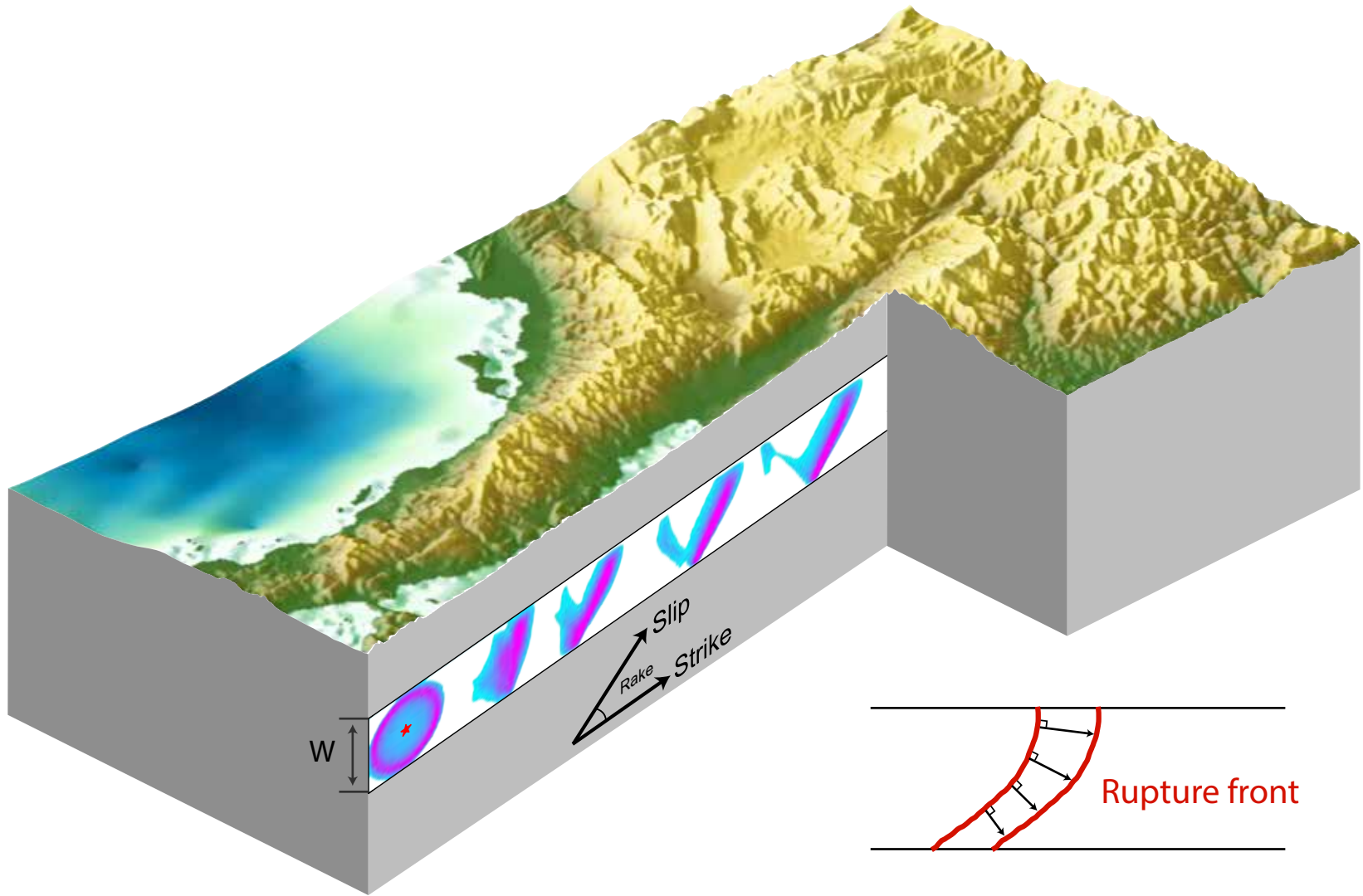
451 **Figure 2** (a) Five different rupture behaviours (see legend) as a function of energy ratio
452 G_c/G_0 and rake angle θ from a systematic set of 3D dynamic rupture simulations. Black
453 curves are the theoretical estimates explained in Methods A4. (b) Normalized depth-
454 averaged rupture speed v_r/v_S (colored curves coded by rake angle) as a function of
455 normalized distance L/W from models with $G_c/G_0 = 0.63$. v_R , v_S , v_E , and v_P are the
456 Rayleigh wave, shear wave, Eshelby, and P wave speeds, respectively. (c) Depend-
457 cies of normalized steady supershear speed (depth-averaged) on energy ratio and rake
458 angle. (d) Dependencies of real speed angle (depth-averaged) on energy ratio and rake
459 angle. Note that the real speed angle has opposite rotation relative to the rake angle.
460 Gray region indicates subshear ruptures whose real speed angle is smaller than 5° .

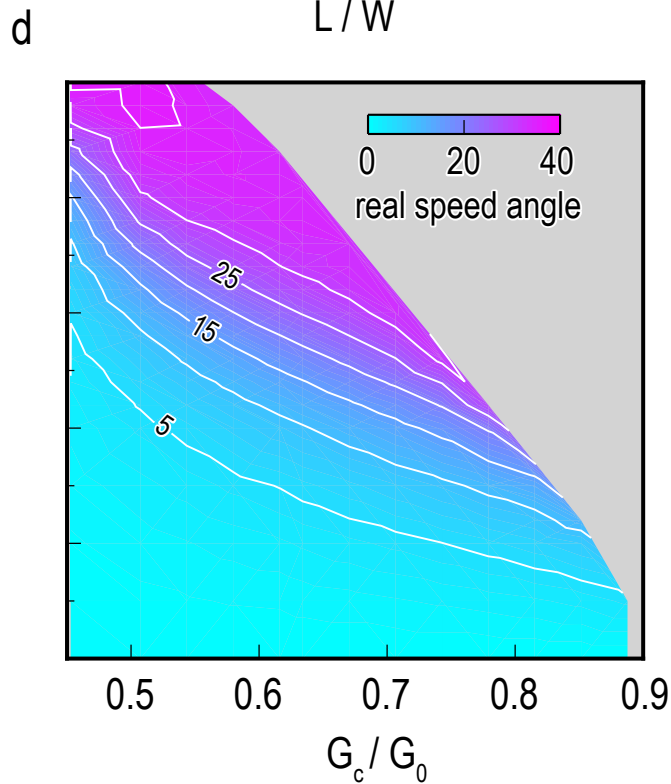
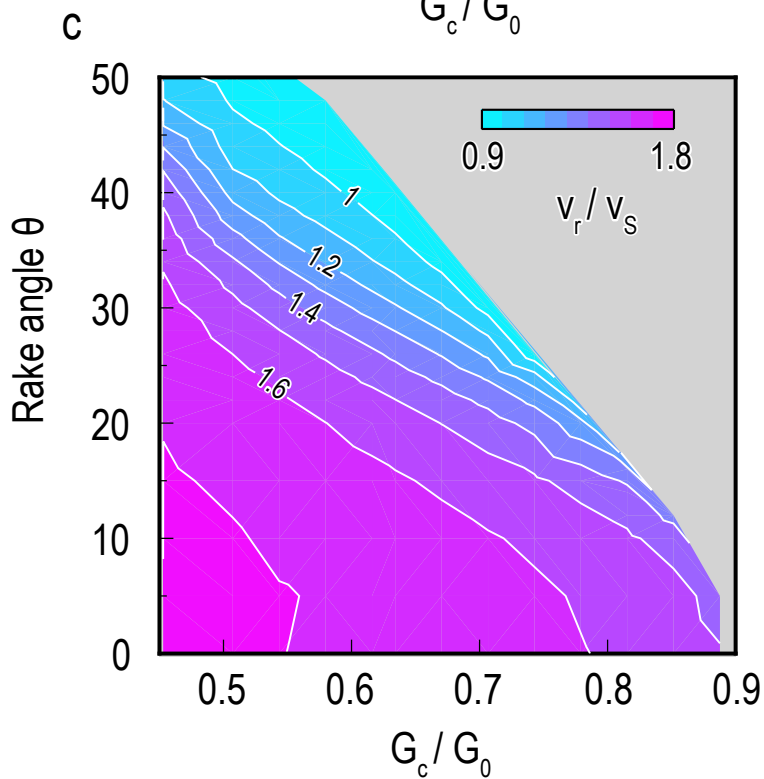
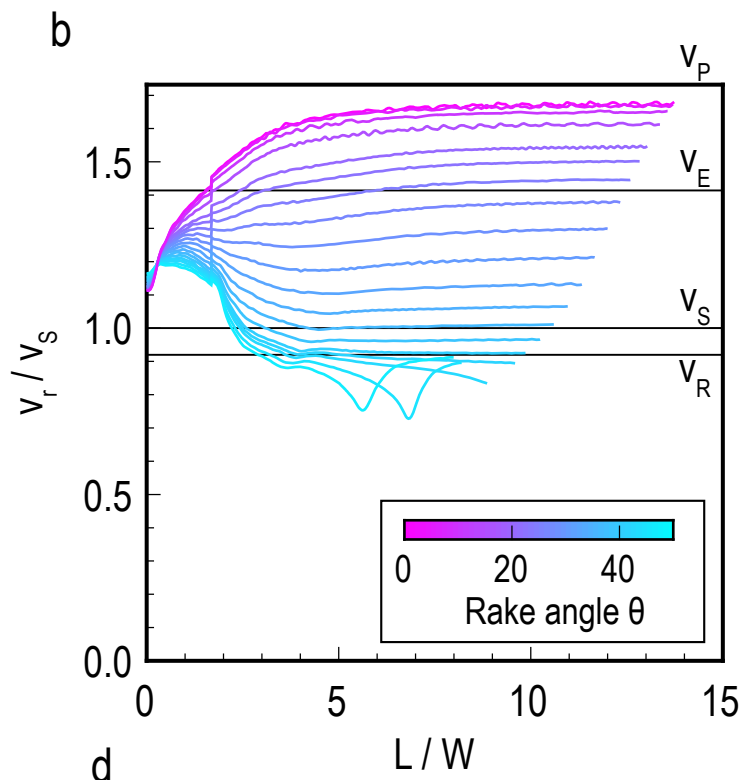
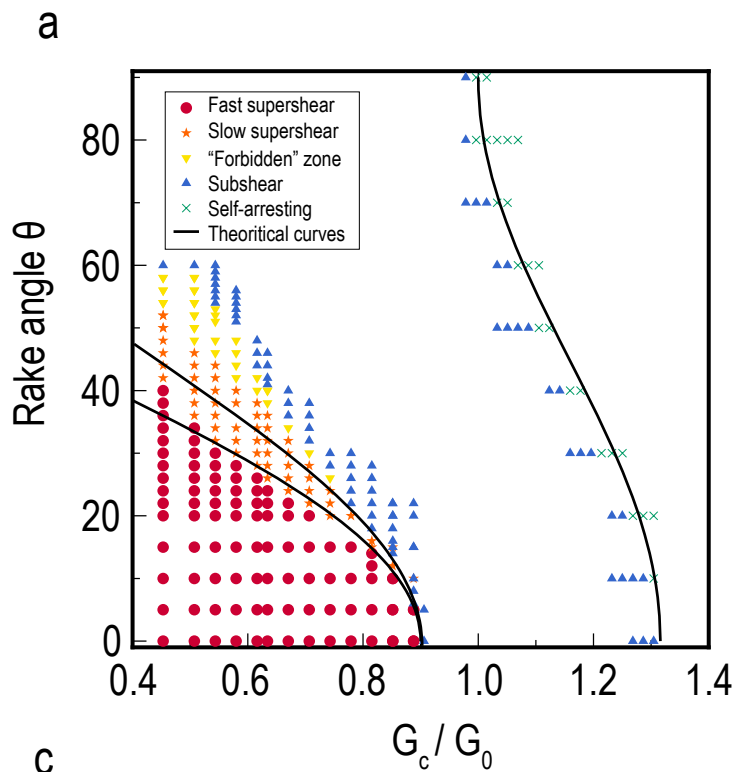
461 **Figure 3** (a) Observed rupture speed and rake angle of global earthquakes (colored
462 symbols coded by aspect ratio). The rupture speeds are compiled from various references⁴⁻¹¹.
463 The rake angles and the aspect ratios are compiled from USGS and SRCMOD¹³. The
464 shear wave speeds used to normalize the rupture speed are either from their original
465 papers or from 1D PREM model. The events with unknown aspect ratios are presented
466 as white symbols. Black solid curves indicate the contours of energy ratio (>0.5) in 3D
467 numerical simulations. Black dash curves and arrow indicate qualitatively the position of

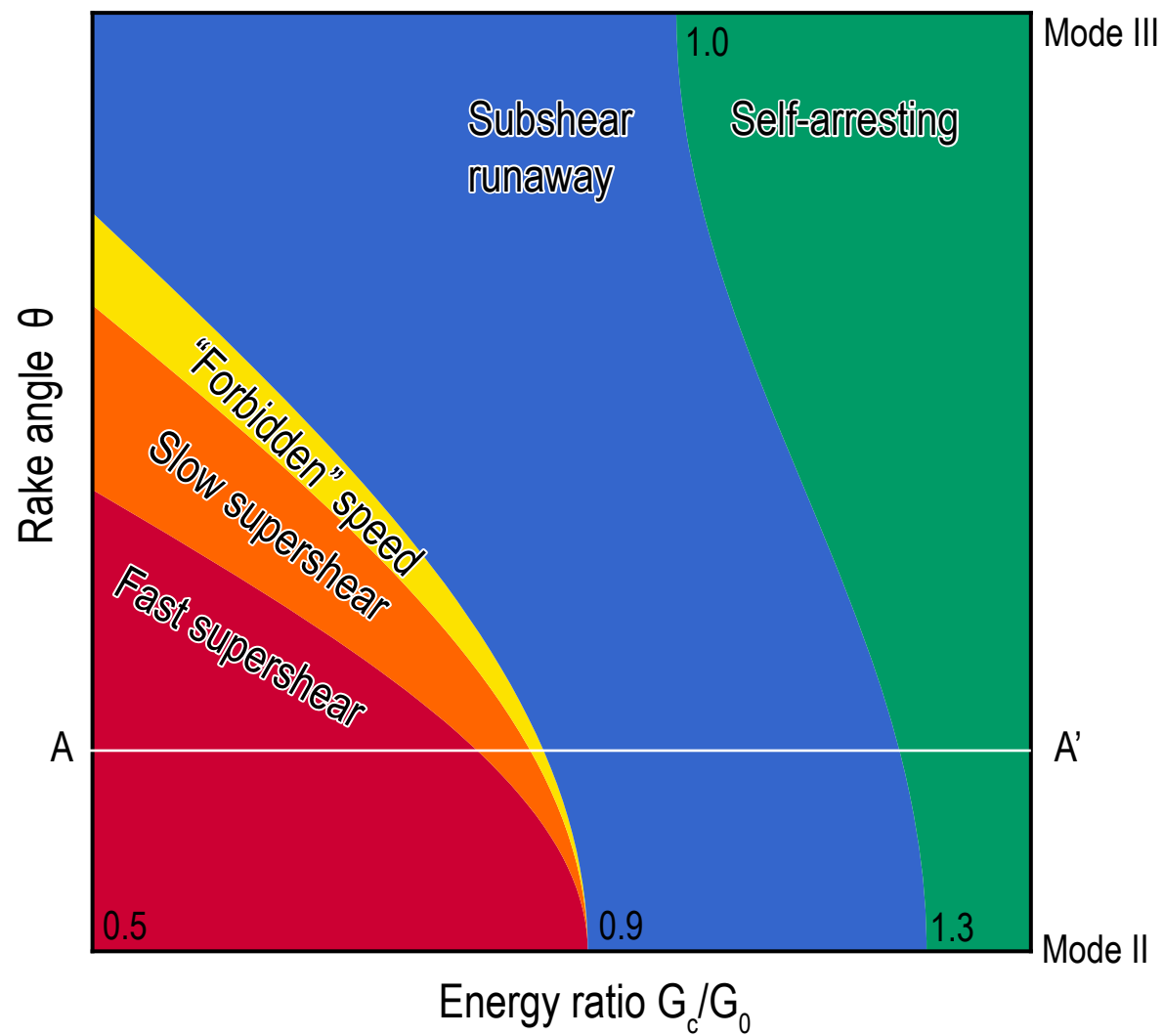
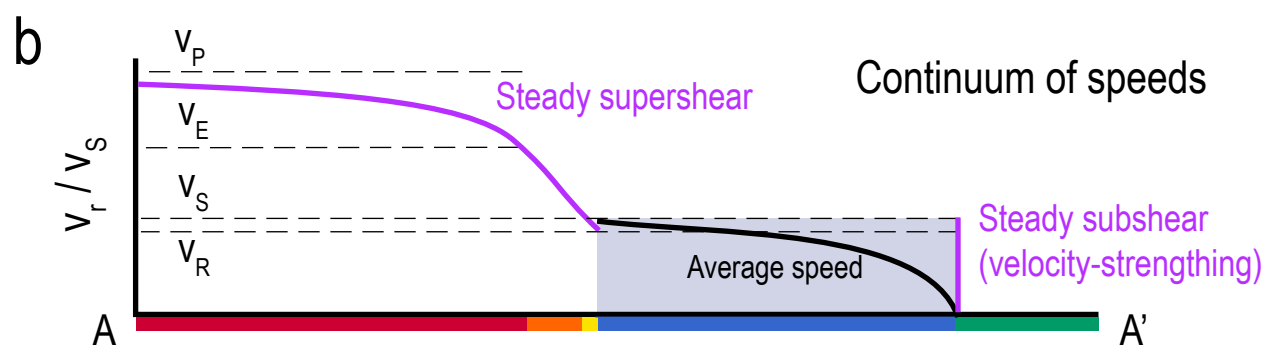
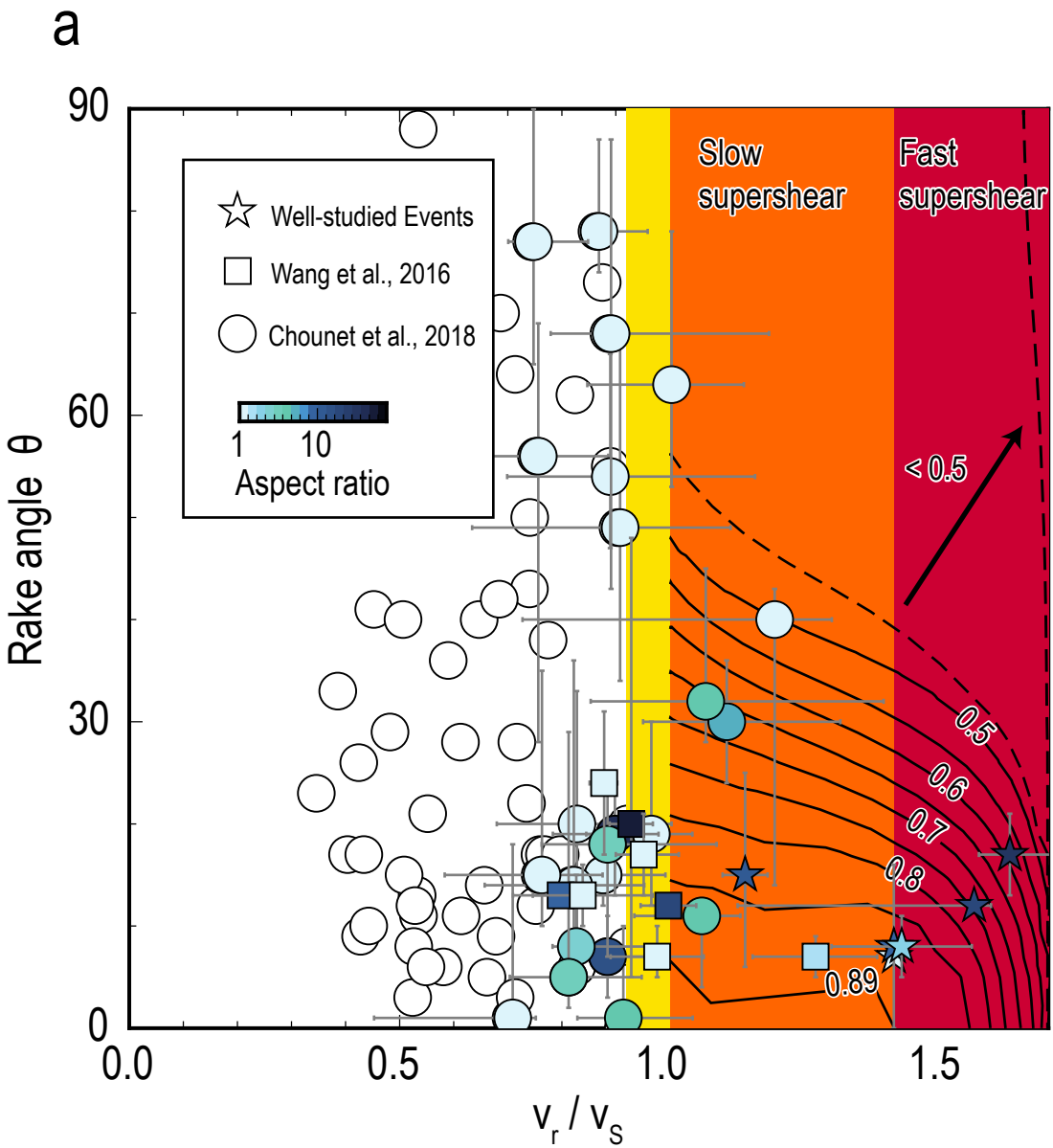
468 contours for smaller energy ratios (<0.5) deduced from theory (Methods A1). (b) Bottom:
469 cartoon showing five different rupture behaviours in $(G_c/G_0, \theta)$ space derived from the 3D
470 numerical simulations and theory. Numbers indicate the critical energy ratios at several
471 points. Top: continuum of steady and average rupture speed as a function of energy ratio
472 for a fixed rake angle as shown in the profile AA' in the bottom plot. Purple curves indi-
473 cate the steady-state rupture speeds. Black curve indicates the average rupture speeds
474 as a function of energy ratio, with fixed rupture length and initial rupture speed. Gray box
475 shows all possible average rupture speeds for various rupture length and initial rupture
476 speed.

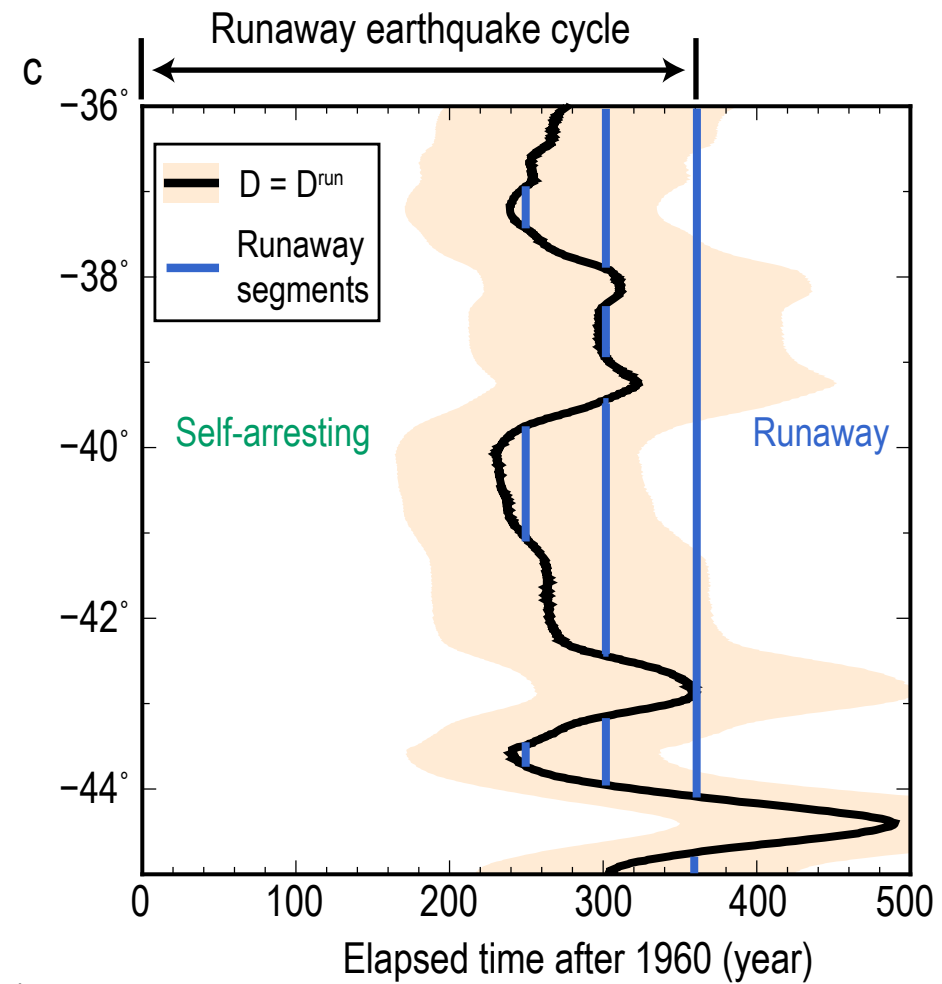
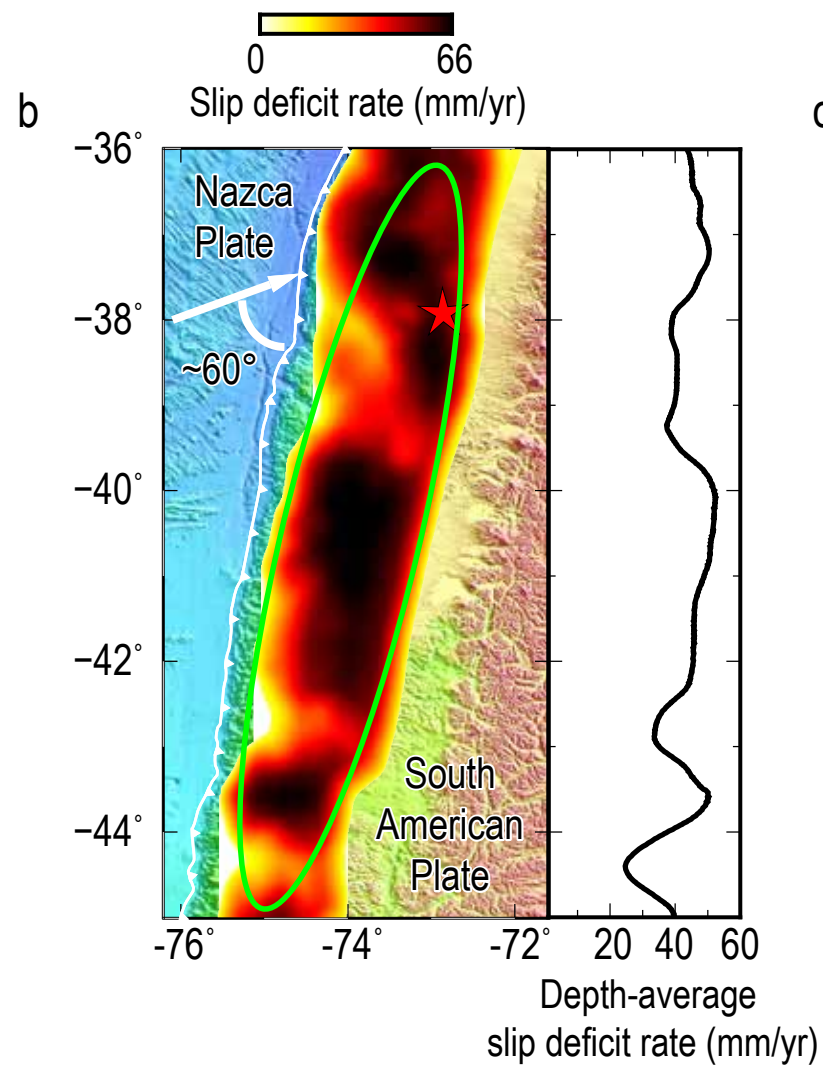
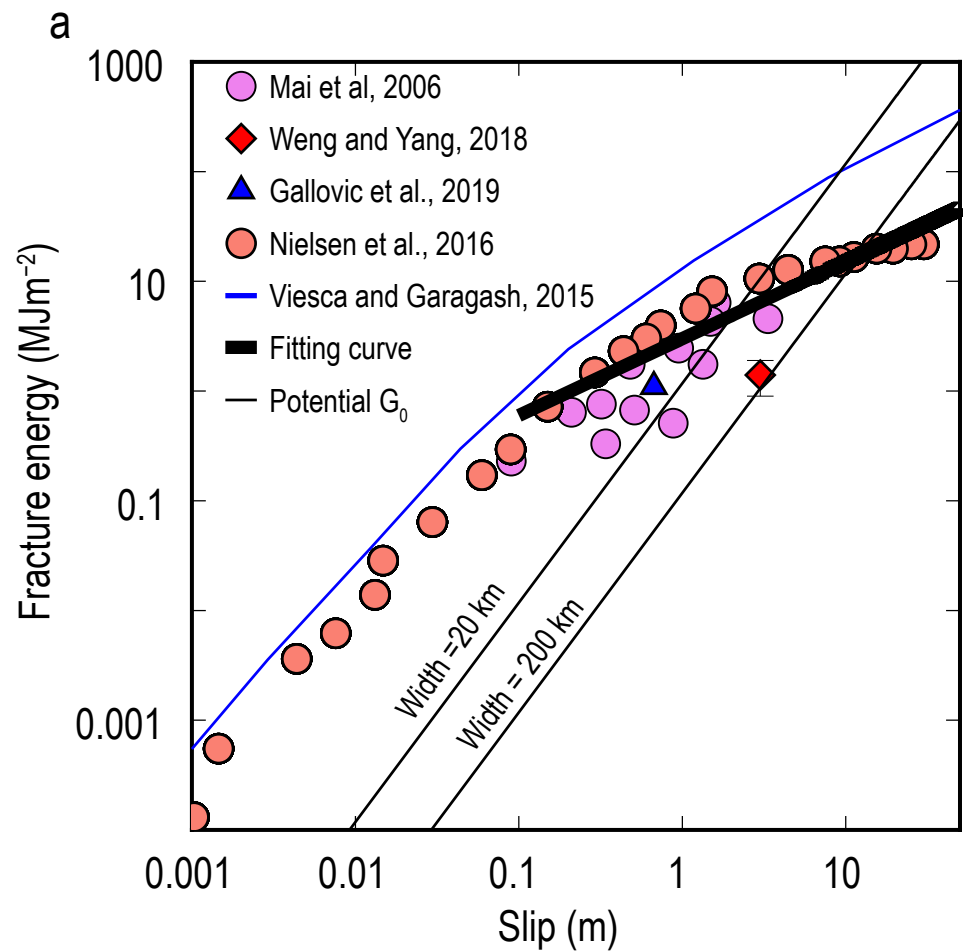
477 **Figure 4** (a) Estimated fracture energy G_c versus final slip D over a wide range of event
478 sizes derived from various references^{21–25}, laboratory experiments²⁴. The black thick line
479 is the power-law fitting curve for the results of dynamic models and lab experiments with
480 $D > 0.1m$. The thin black lines are the theoretical relations between energy release rate
481 G_0 and final slip D on long faults for different seismic widths. (b) Distribution of slip deficit
482 rate of the southern Andes subduction zone, Chile (left) and depth-averaged slip deficit
483 rate along strike (right). The slip deficit rate is the product of a seismic coupling model
484 inferred from geodetic data²⁸ and a constant plate convergence rate ~ 66 mm/yr. The epi-
485 center (red star) and rough rupture region (green curve) of the 1960 Valdivia earthquake
486 are shown. The rake angle between the Nazca Plate convergence and strike direction
487 is $\sim 60^\circ$. (c) Elapsed time for the fault to accumulate the critical slip deficit for runaway
488 rupture, $D = D^{run}$, after the 1960 earthquake that is assumed to have released all the slip

489 deficit. The colored band accounts for uncertainties in the $G_c - D$ scaling relation. The
490 fault is partitioned into segments with runaway and self-arresting behavior, and this seg-
491 mentation evolves with time (runaway segments are shown by blue lines at three times).









Oblique slip on long faults enables a continuum of earthquake rupture speeds

Huihui Weng¹ and Jean-Paul Ampuero¹

¹*Université Côte d'Azur, IRD, CNRS, Observatoire de la Côte d'Azur, Géoazur, 250 rue Albert Einstein, Sophia Antipolis, 06560 Valbonne, France*

Contents

4 Supplementary Figures

Figure S1.

Figure S2.

Figure S3.

Figure S4.

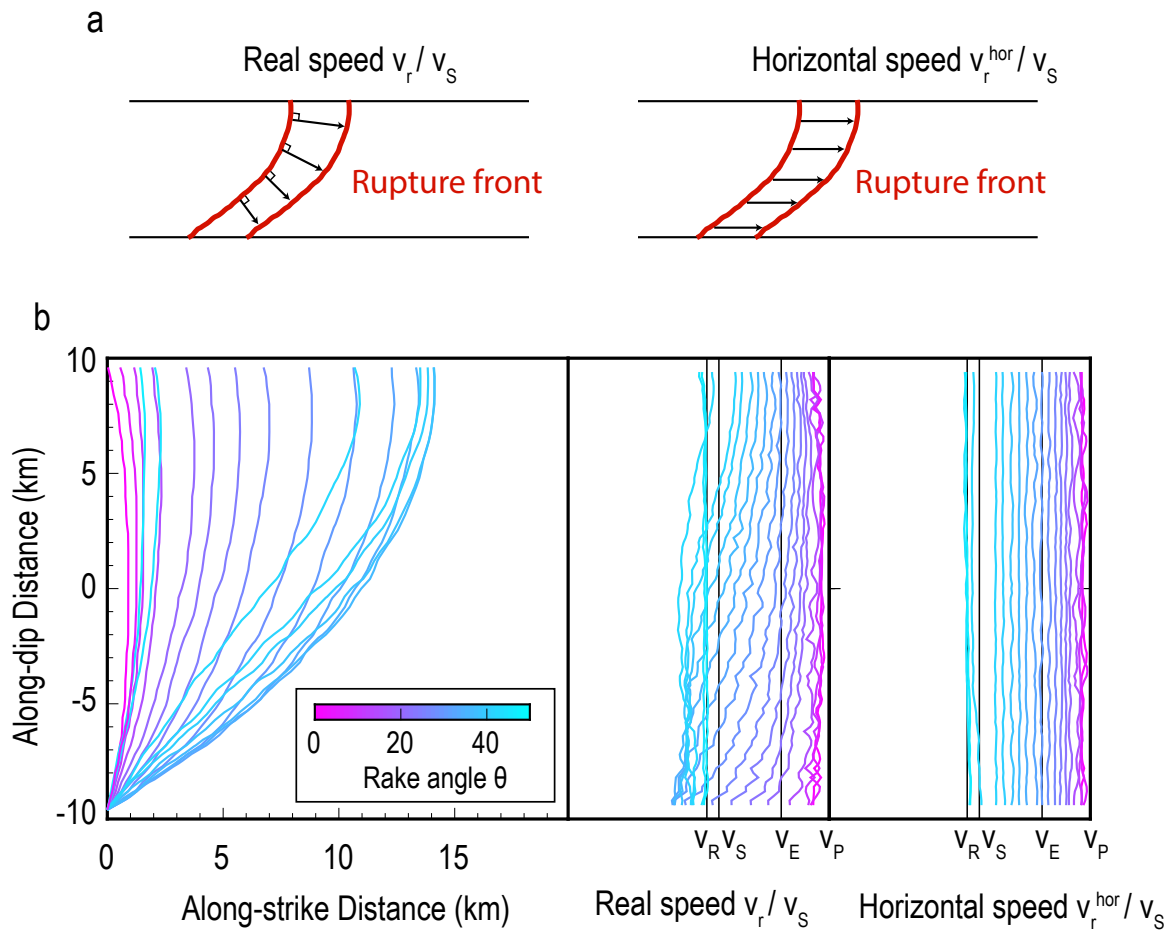


Figure S1: (a) The definition of real speed and apparent horizontal speed. (b) The shape (left), distributions of real speed (middle) and horizontal speed (right) of steady rupture fronts across the depth (colored symbols coded by rake angle).

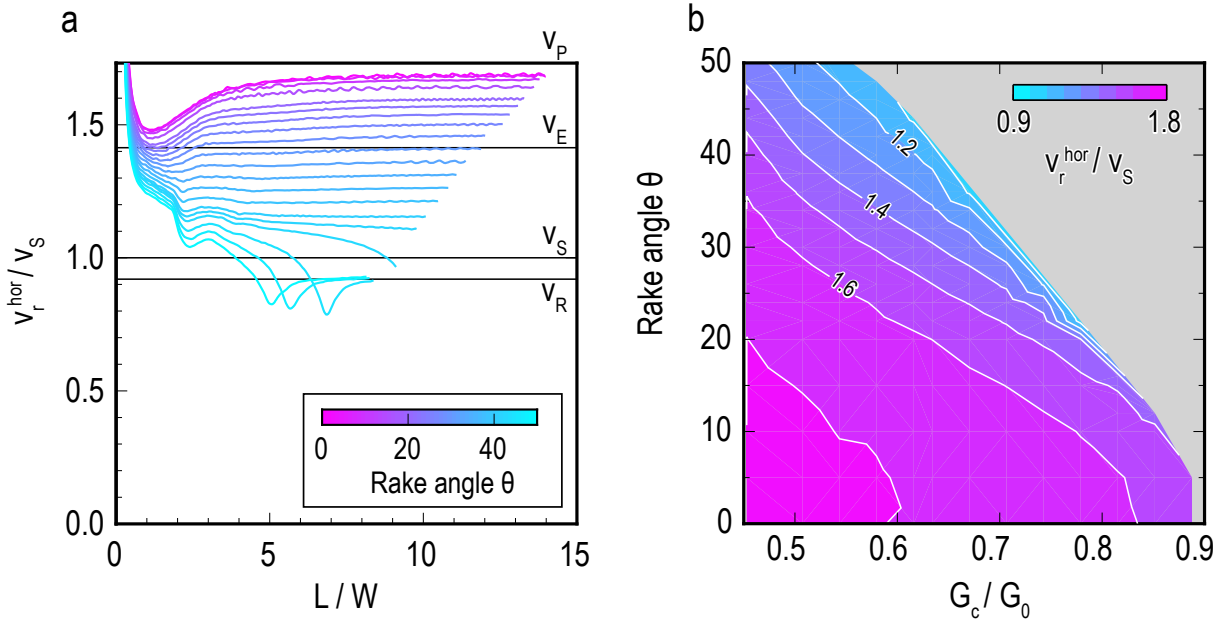


Figure S2: (a) Normalized depth-averaged horizontal speed v_r^{hor} (colored curves coded by rake angle) as a function of normalized distance L/W from the 3D dynamic rupture simulations with $G_c/G_0 = 0.63$. (b) Dependencies of normalized depth-averaged horizontal speed on energy ratio and rake angle.

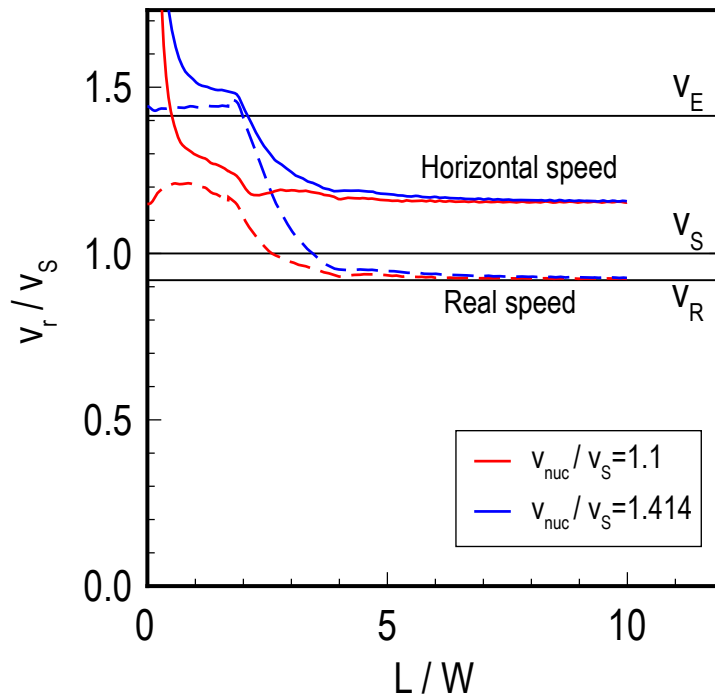


Figure S3: Normalized depth-averaged speeds as a function of normalized distance L/W from the 3D dynamic rupture simulations with different nucleation speeds.

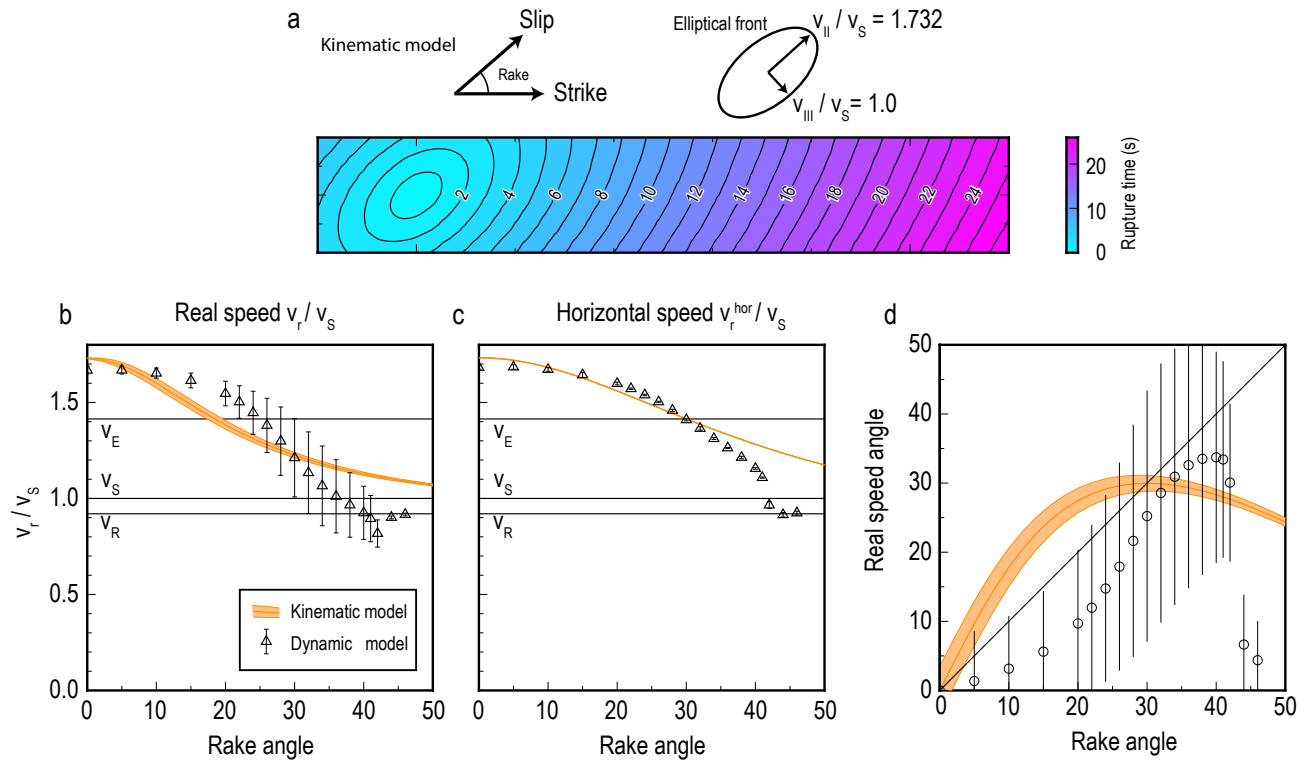


Figure S4: (a) Rupture contours of a kinematic model with oblique slip whose rupture extends as an elliptical front propagating at the P wave speed along its major axis and at the S wave speed along its minor axis. The rake angle is the angle between the major axis of the ellipse and the strike direction. (b) The comparison of depth-averaged real speed between the kinematic and dynamic models with $G_c/G_0 = 0.63$ versus rake angle. The definition of real speed and horizontal speed are the same for both the kinematic and dynamic models. (c) The comparison of horizontal speed versus rake angle. (d) Dependency of depth-averaged real speed angle on rake angle for both kinematic and dynamic models.